A Novel All-Optical Sensor Design Based on a Tunable Resonant Nanocavity in Photonic Crystal Microstructure Applicable in MEMS Accelerometers

Mojtaba HOSSEINZADEH SANI[1], Hamed SAGHAEI[2*],
Mohammad Amin MEHRANPOUR[3], and Afsaneh ASGARIYAN TABRIZI[4]

[1]*Department of Electrical Engineering, Imam Reza International University, Mashhad 9138833186, Iran*

[2]*Department of Electrical Engineering, Shahrekord Branch, Islamic Azad University, Shahrekord 8813733395, Iran*

[3]*Department of Electrical Engineering, Sari Branch, Islamic Azad University, Sari 4816119318, Iran*

[4]*Academic Center for Education, Culture, and Research (ACECR), Tabriz 5156845195, Iran*

*Corresponding author: Hamed SAGHAEI   E-mail: h.saghaei@iaushk.ac.ir

Abstract: In view of the large scientific and technical interest in the microelectromechanical system (MEMS) accelerometer sensor and the limitations of capacitive, resistive piezo, and piezoelectric methods, we focus on the measurement of the seismic mass displacement using a novel design of the all-optical sensor (AOS). The proposed AOS consists of two waveguides and a ring resonator in a two-dimensional rod-based photonic crystal (PhC) microstructure, and a holder which connects the central rod of a nanocavity to a proof mass. The photonic band structure of the AOS is calculated with the plane-wave expansion approach for TE and TM polarization modes, and the light wave propagation inside the sensor is analyzed by solving Maxwell's equations using the finite-difference time-domain method. The results of our simulations demonstrate that the fundamental PhC has a free spectral range of about 730 nm covering the optical communication wavelength-bands. Simulations also show that the AOS has the resonant peak of 0.8 at 1.644 μm, quality factor of 3288, full width at half maximum of 0.5 nm, and figure of merit of 0.97. Furthermore, for the maximum 200 nm nanocavity displacements in the x- or y-direction, the resonant wavelengths shift to 1.618 μm and 1.547 μm, respectively. We also calculate all characteristics of the nanocavity displacement in positive and negative directions of the x-axis and y-axis. The small area of 104.35 μm^2 and short propagation time of the AOS make it an interesting sensor for various applications, especially in the vehicle navigation systems and aviation safety tools.

Keywords: Photonic crystal; MEMS; accelerometer sensor; tunable resonator; finite-difference time-domain method

1. Introduction

Photonic crystals (PhCs) can be used as appropriate structures for creating all-optical systems and networks due to the low loss and high capability in guiding and controlling the light [1, 2].

They consist of a periodic arrangement of materials with high and low refractive indices. PhCs in two forms of dielectric rods in the air bed and air holes in the dielectric slab are used to control and guide the flow of light in the PhC microstructure. The photonic bandgap (PBG) is a range of wavelengths that cannot be propagated in the structure. It is due to the destructive interference that occurs between emitting and reflective waves in the boundaries where the refractive index changes. Thus, waveguides in a PhC can be created by removing one or more rows of dielectric rods. PhC-based structures are excellent choices for designing many types of optical devices such as optical filters [3–8], PhC fibers [9–18], multiplexers and demultiplexers [19–26], encoders and decoders [27–30], switches [31–36], logic gates [37–42], analog to digital converters (ADCs) [43–49], and sensors [50–57]. In recent years, photonic sensors have been widely studied and fabricated because of the increasing demand for sensing applications in the health care, food quality, control defense, security, automobiles, aerospace, and so on. Accelerometer sensors are widely used in many electronic devices, as well as vehicle vibration control, aerospace, and navigation systems [58–60]. Many manufacturers have been commercialized as high-performance microelectromechanical system (MEMS) inertial sensors for many applications [61–65]. MEMS accelerometer is one of the most popular types of displacement sensors [66–68]. An optical MEMS is a combination of three micro-optical technologies, micro-mechanics, and microelectronics [69–71]. The combination of these technologies offers the advantage of using less force to move more, which makes the MEMS system more sensitive because photons have zero mass.

The development of MEMS sensors has reduced the size and power consumption of older sensors. MEMS accelerometers have been used in navigation systems and aviation safety tools. Such accelerometers are usually based on a micro- or nano-meter displacement of a holder. Several methods have been presented so far to measure the displacement of seismic mass, such as capacitive [72, 73], resistive piezo [74], piezoelectric [75], and optical [76, 77]. The capacitive sensing technology is very attractive in the applications because of its ease of implementation compared with other sensing technologies. However, this method has some drawbacks such as the curling effect [78], the effect of parasitic capacitance, and small variations in capacitance [79] under the mechanical load, in which they limit the accuracy and speed of the device. Studies illustrate that optical sensing methods have better performance in terms of resolution and sensitivity compared with the other existing sensing techniques [59].

Furthermore, the methods based on optical measurements are more reliable due to their immunity against electromagnetic interferences (EMI), which makes them suitable tools in EMI contaminated environments [80]. The operational principle of optical MEMS accelerometers is based on the modulation of lightwave properties such as intensity, and phase and wavelength modulation under applied acceleration [58, 76, 81]. Nie *et al.* [82] proposed an optical MEMS accelerometer sensor based on a one-dimensional photonic crystals wavelength modulation system with a focus on optimizing the sensitivity of the high-frequency device. A very large bandwidth, an excellent sensitivity to optical sensing, and a considerable resolution of the high-frequency device of the proposed sensor provided several attractive performance aspects.

The current study presents a novel accelerometer sensor in a two-dimensional PhC. The advantages of this device are the wide free spectral range (*FSR*), narrow full width at half maximum (*FWHM*), high figure of merit (*FOM*), small footprint, and relatively low production cost compared with other existing MEMS sensors that make it an appropriate device for sensing applications. In fact, the resonant

Mojtaba HOSSEINZADEH SANI *et al.*: A Novel All-Optical Sensor Design Based on a Tunable Resonant Nanocavity in Photonic Crystal Microstructure Applicable in MEMS Accelerometers

459

wavelength of the proposed structure changes when the central nanocavity moves in every direction of the *x* and *y*-directions. The rest of this paper is organized as follows: In Section 2, the photonic band structure of the rod-based PhC is calculated for TE and TM modes, and in Section 3, the novel structure of the accelerator sensor is proposed, and the transmission spectrum is plotted. The numerical results accompanied by discussion are given in Section 4, and finally, we conclude the paper in Section 5.

2. Modeling of PhC-based structure

The structure is designed of silicone rods in the air bed. The inset of Fig. 1(a) demonstrates a hexagonal lattice of the fundamental two-dimensional PhC that is used in this study. The refractive index and the radius of the dielectric rods are assumed to be *n* = 3.6 and *r* = 100 nm, respectively [64]. The band structure of the fundamental PhC has been calculated employing the plane wave expansion method (PWE) and plotted in Fig. 1(a) for TM and TE polarization modes considering that a lattice constant is called the center-to-center distance of the two adjacent dielectric rods of *a* = 500 nm. It demonstrates that there are wide and narrow PBGs in TM and TE polarization modes, respectively. Figure 1(b) shows the transmission spectra and field distributions of the TE and TM modes of the fundamental PhC. It represents that the widest bandgap is achieved in the range of $a/\lambda = 0.266 - 0.435$ (corresponding to the wavelength range of $\lambda = 1.14\,\mu m - 1.87\,\mu m$) for the TM mode with a broad *FSR* of about 730 nm. It is an appropriate bandwidth for designing all-optical devices in the C-band communication window. The insets demonstrate the distributions of the electric (TE mode) and magnetic (TM mode) fields at the wavelength of 1.644 μm along the *x*-axis. As seen in the figure, the TE mode propagates in the fundamental PhC, while the TM mode cannot be emitted in the structure. Therefore, by creating different defects in the structure, we try to direct the

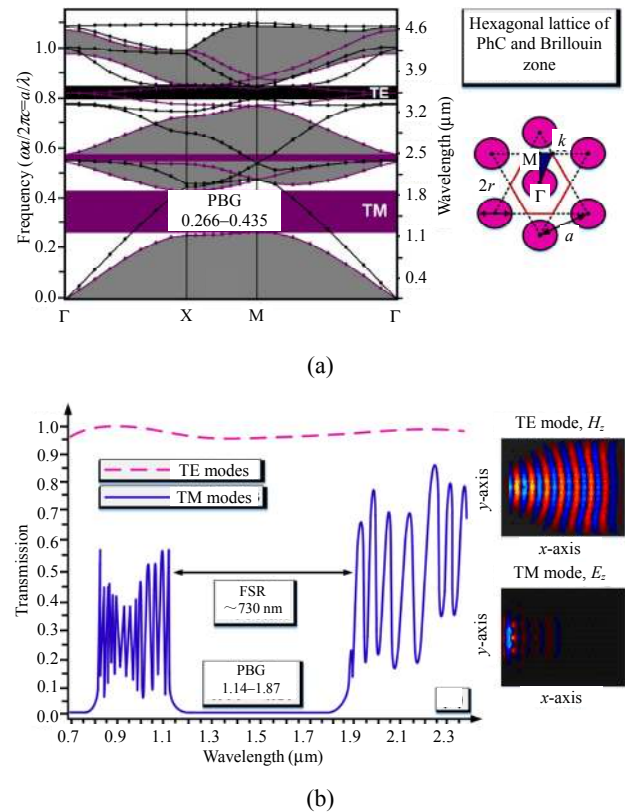light wave to the desired output.

(a)

(b)

Fig. 1 Results of (a) photonic band structure of a fundamental PhC for TM (violet) and TE (dark gray) polarization modes (the inset shows a hexagonal lattice of the fundamental PhC used in this study) and (b) transmission versus wavelength for TM (blue) and TE (pink) modes [the insets demonstrate the distributions of the magnetic (TE mode) and electric (TM mode) fields at the wavelength of 1.644 μm along the *x*-axis].

3. Proposed all-optical sensor

Although the PhC size reduction leads to a decrease in the light wave propagation time, it significantly increases the waveguide loss and also decreases the sensitivity and quality factor of the device. In this study, we aim to design a high-speed as well as low-loss all-optical sensor (AOS) using a PhC-based nanocavity resonator, which yields a high-quality factor as well as a high sensitivity. In Fig. 2(a), we propose an AOS with an area of 104.35 μm². A 19×13 matrix of silicon rods in a hexagonal lattice with a 100 nm rod radius and a 500 nm lattice constant has been used to form the fundamental platform of the structure. The blue dielectric rod with a radius of R_C = 350 nm is the

central resonator used to select the desired wavelength. The integrated input and output waveguides are surrounded by red dielectric rods and closed at the end to increase the reflection of light. All this will increase the intensity of the light and decrease the propagation loss. The green dielectric rods surround the main blue rod to create a narrow-band filter with a high-quality factor for choosing the desired wavelength. The proposed AOS is an ultra-fast device due to choosing short lengths of the waveguides [i.e., W_1 and W_2 shown in Fig. 2(a)]. It has several advantages such as the ease of fabrication because of its small area, inexpensive fabrication processes due to having one layer of

dielectric rods, and high efficiency and flexibility in resonant mode concluded from its multimode nature. Depending on the radius of the central nanocavity, the proposed AOS can separate the resonant wavelengths of the input lightwave propagating through the first waveguide, W_1, and couple them to the output via the second waveguide, W_2. In this device, each resonant mode has a sensitivity and a quality factor proportional to the physical parameters of the AOS, especially its nanocavity. Figure 2(b) shows the transmission spectrum of the AOS. It illustrates that the resonant peak occurs at 1.644 μm in the TM mode. In this wavelength, the AOS has the maximum quality factor.
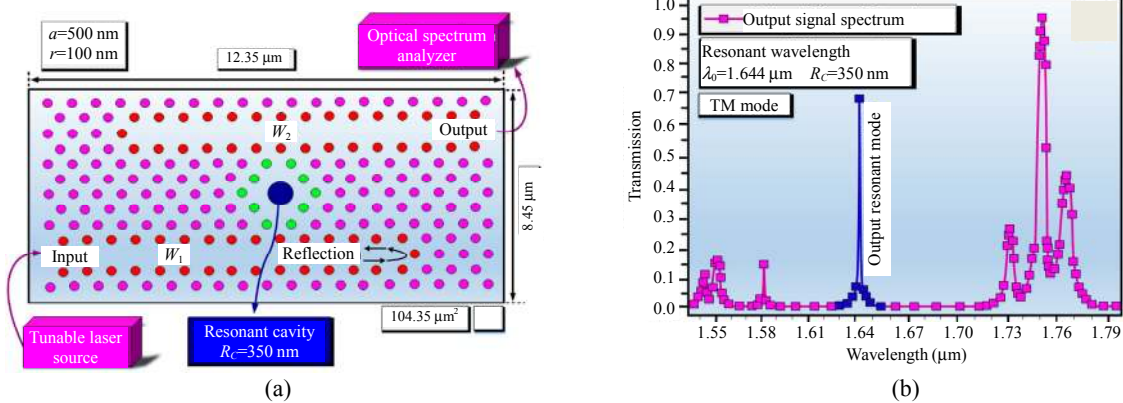

Fig. 2 Illustration of (a) proposed structure of the all-optical sensor based on the nanocavity resonator and (b) wavelength transmission in the TM mode is marked in pink and the output resonance wavelength is marked in blue.

We aim to design an adjustable AOS to measure the displacements of the proof mass. Given the advantages mentioned above, our proposed AOS can be used as the proposed accelerometer displacement measurement system. Figure 3 demonstrates the optical MEMS accelerometer, and the insets show our designed AOS and nanocavity displacement directions.

The main part of the accelerometer consists of the AOS based on the wavelength modulation. It means that the device can detect the displacements of the proof mass by shifting the wavelength of the optical resonant mode. The connected holder to the the proof mass moves the central rod of the nanocavity in the *x*- or *y*- direction depending on the

applied force, and the central resonant wavelength is shifted. In this design, the displacement sensing system is a mechanically adjustable AOS. The optical signal of the laser source is launched into the input waveguide of the AOS, then it is selected by the central resonant nanocavity and finally coupled to the output. Sheikhaleh *et al.* [76] presented an optical MEMS accelerometer using an add-drop filter (ADF) in the microstructured PhC. In this device, when an acceleration is applied to the proof mass and it is along the positive *y*-direction (+*y*), the holder is displaced in the opposite *y*-direction (–*y*). In the proposed AOF in [76], it is not possible to detect displacement along the *x*-axis. But the proposed AOS, shown in Fig. 3, can detect the

Mojtaba HOSSEINZADEH SANI *et al.*: A Novel All-Optical Sensor Design Based on a Tunable Resonant Nanocavity in Photonic Crystal Microstructure Applicable in MEMS Accelerometers

461

displacement of the holder attached to the proof mass in all directions.
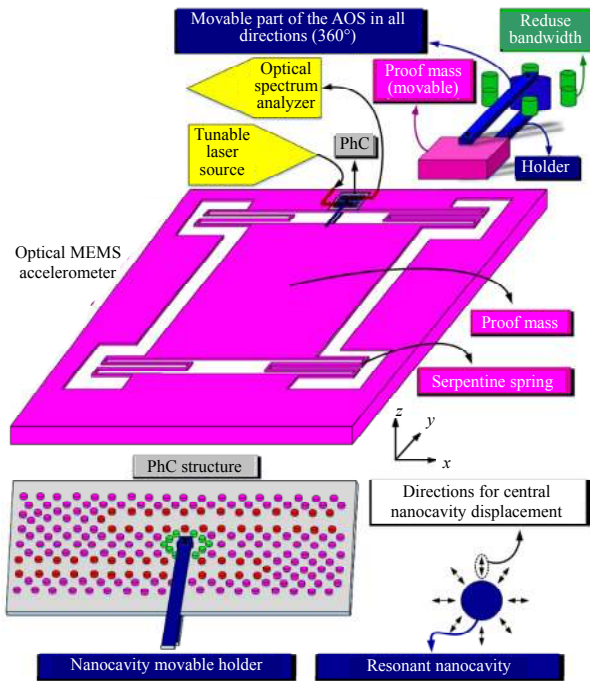

Fig. 3 Proposed optical MEMS accelerometer. The insets demonstrate our designed AOS and nanocavity displacement directions.

4. Numerical results and discussion

Figure 4 represents that the proposed central nanocavity can be mechanically moved in all directions. Our purpose in the AOS design is to detect the acceleration of the mass attached to the accelerometer. In Fig. 4(a), the central nanocavity is displaced by the holder in the positive direction ($+x$) and in Fig. 4(b), the displacement path is in the negative direction ($-x$). The displacement of the dielectric rod along the x-axis from the center of the resonator is defined by Δx that its maximum value is 200 nm. In Figs. 4(c) and 4(d), the central nanocavity is displaced by the holder in the positive direction ($+y$) and negative direction ($-y$), respectively. Δy is the displacement of the dielectric rod in the AOS along the y-axis from the center of the resonator. In this study, it has a maximum value of 200 nm.

The AOS operates based on the calculation of the transmission profile in terms of wavelength. As the location of the nanocavity shifts, the transmission changes. The quality factor of this sensor is defined as follows:

$$Q_f = \lambda / FWHM \qquad (1)$$

where λ represents the resonant wavelength. It is a standard way of describing the transmission characteristics of an optical sensor. Indeed, a filter with a wider *FWHM* allows more of the spectrum to pass, but it is less wavelength-selective. *FWHM* is one of the key parameters of the proposed sensor design and determines the sensor detection limit. According to (1), the quality factor is inversely proportional to *FWHM*.

It means that finding an appropriate PhC structure with a short bandwidth is necessary to increase the quality factor and detection limit (the minimum physical displacement detectable by the sensor). Also, it is worthy to note that the increased *FWHM* increases the AOS loss because other wavelengths are not allowed to propagate in the narrowband AOS; they are therefore lost in the form of heat. It is necessary to select a sufficiently wide *FSR* sensor. It ensures that the adjacent resonant peaks do not interfere with the working resonant peak. In the longer wavelengths, *FSR* is greater because *FSR* is directly proportional to the square of the resonance wavelength. Since longer wavelengths have a greater impact on *FSR*, the sensor design at longer wavelengths is the most basic way to optimize *FSR*. Therefore, the accelerometer based on the resonant wavelength shift approach requires a wider *FSR* that is achieved by the proposed AOS in this study. The accelerometer sensor sensitivity is defined by [83]

$$S = \Delta \lambda / \Delta x \qquad (2)$$

where Δx is the displacement path in the x-direction, and $\Delta \lambda$ is the wavelength shift representing the difference between the resonant frequencies of the two outputs. *FOM* is a key parameter for describing

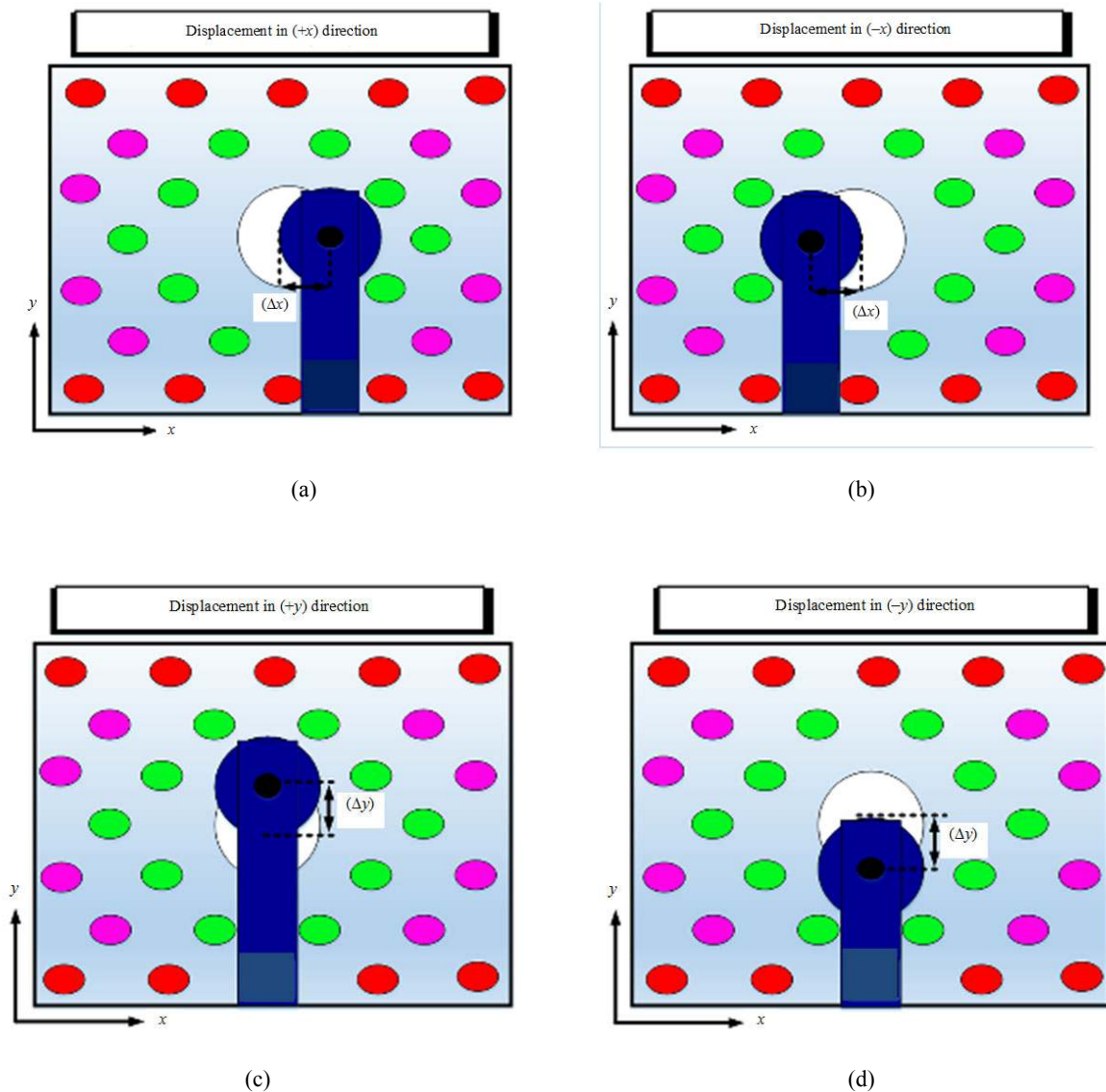the sensing capability of the device that is given by

$$FOM = S/FWHM . \tag{3}$$

(a)

(b)

(c)

(d)

Fig. 4 Displacements of the nanocavity in (a) +*x*, (b) −*x*, (c) +*y*, and (d) −*y* directions.

An optical signal is launched into the device using a continuous wave adjustable laser source, and the outputs are monitored using an optical spectrum analyzer.

Figure 5(a) shows the transmission spectra for the displacements along the *x*-axis from −200 nm to 200 nm. When the nanocavity is at the center of the structure (called Case-A), its normalized transmission spectrum, shown by pink, has a peak of 0.8 (called P_{CE} = 0.8) at λ = 1.644 μm. When the central nanocavity moves 200 nm along the positive

direction of the *x*-axis (Case-B), the resonant peak, shown by blue, becomes 0.66 (P_{CE} = 0.66) and also shifts toward λ = 1.618 μm while a 200 nm displacement in the negative direction of the *x*-axis (Case-C) results in the peak value increasing to 1 (P_{CE} = 1). The difference between the resonant wavelengths for 0 nm and 200 nm displacements is $\Delta\lambda$ = 26 nm. Therefore, the sensitivity parameter ($\Delta\lambda/\Delta x$) of this sensor is *S* = 0.13. For accurate calculations of the sensor parameters of the cases mentioned above, we plot the log scale transmission

Mojtaba HOSSEINZADEH SANI *et al.*: A Novel All-Optical Sensor Design Based on a Tunable Resonant Nanocavity in Photonic Crystal Microstructure Applicable in MEMS Accelerometers

463

spectra of Case-A, Case-B, and Case-C in Figs. 5(b) – 5(d). Figure 5(b) demonstrates in Case-A that the resonant nanocavity is in the center of the resonator, the resonant wavelength is λ=1.644 μm, *FWHM* is 0.5 nm, and then according to (1), the quality factor will be 3 288. By calculating the sensitivity and

FOM using (2) and (3), their values will be 0.485 and 0.97, respectively. As seen in Fig. 5(c), Case-B has the resonant wavelength, *FWHM*, quality factor, and *FOM* of 1.618 μm, 0.8 nm, 2 022, 0.162 5, respectively.
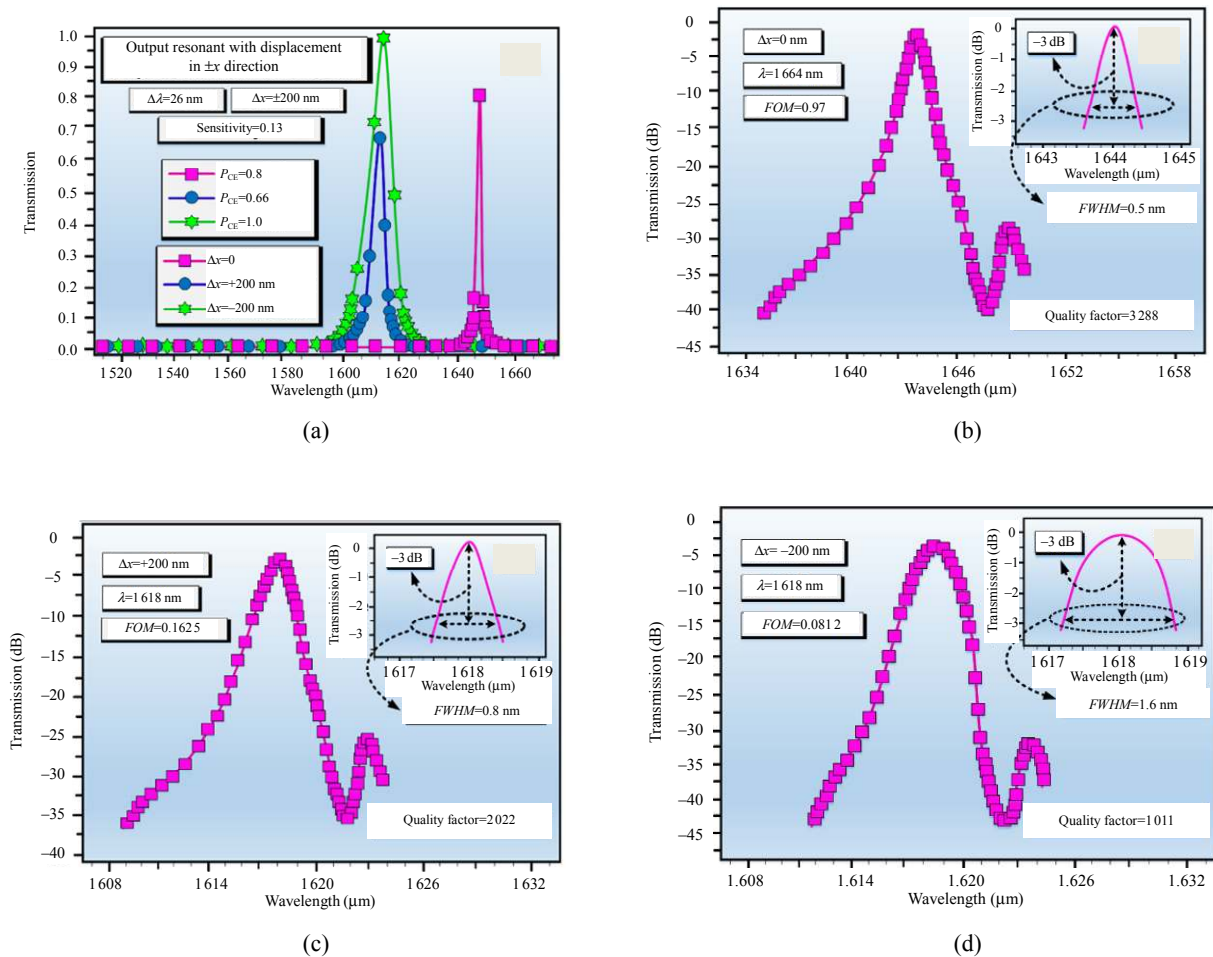

(a)

(b)

(c)

(d)

Fig. 5 Results of (a) transmission spectra of Case-A, Case-B, and Case-C, and transmissions in dB of (b) Case-A, (c) Case-B, and (d) Case-C.

Figure 5(d) illustrates that Case-C has the resonant wavelength equal to that of Case-B. According to the figure, *FWHM*, quality factor, and *FOM* of Case-C are 1.6 nm, 1 011, 0.081 2, respectively. We also study the effect of displacements along the *y*-axis on the sensor parameters. Figure 6(a) demonstrates the transmission spectra for displacements along the *y*-axis from –200 nm to 200 nm. As we mentioned

earlier, when the nanocavity is at the center of the resonator (Case-A), its normalized transmission spectrum, shown by pink, has a peak of 0.8 at λ=1.644 μm.

When the central nanocavity moves 200 nm in the positive *y*-direction, (Case-D), the peak of the normalized transmission spectrum, shown by blue, shifts toward λ=1.547 μm while a 200 nm displacement in the negative *y*-direction (Case-E)

results in the peak value of the normalized transmission spectrum becoming 0.58 (P_{CE} = 0.58). The difference between the resonant wavelengths for the 0 nm and 200 nm displacements is $\Delta\lambda$ = 97 nm. Therefore, the sensitivity parameter ($\Delta\lambda/\Delta y$) of this sensor is S = 0.485. Figure 6(c) represents in Case-D that λ = 1.547 μm. In this case, *FWHM* increases to 1.0 nm, which reduces the quality factor and *FOM* to 1547 and 0.485, respectively. Figure 6(d) shows in Case-E, the resonant wavelength is equal to the resonant wavelength of Case-B, i.e., λ = 1.547 μm. In this case, *FWHM*, quality factor, and *FOM* are 1.4 nm, 1031, and 0.346, respectively. Figure 7 demonstrates the lightwave propagation inside the AOS fo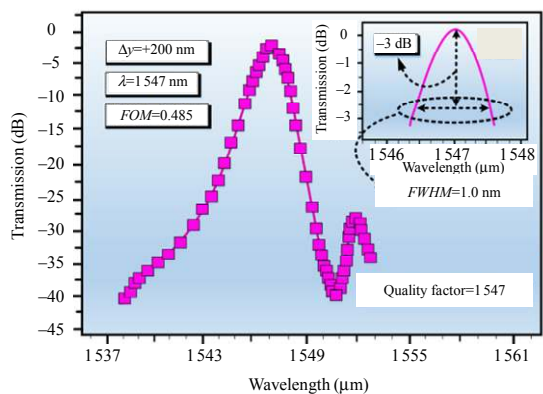r the nanocavity displacements in the x-direction and y-direction. Figure 7(a) shows that for the –200 nm displacement of the nanocavity in the y-direction, the transmission at the resonant wavelength of 1547 nm is 58%. Figure 7(b) represents the light propagation in the AOS for the –200 nm displacement in the x-direction in which all incoming light at 1618 nm passes through the structure. Figures 7(c) and 7(d) illustrate that for the non-displacement of the nanocavity, the transmission is 80% at 1644 nm. Furthermore, Fig. 7(e) illustrates a 200 nm displacement in the x-direction results in a 100% transmission at 1547 nm and Fig. 7(f) shows for the 200 nm displacement of the nanocavity in the x-direction, the transmission is 66% at 1618 nm.
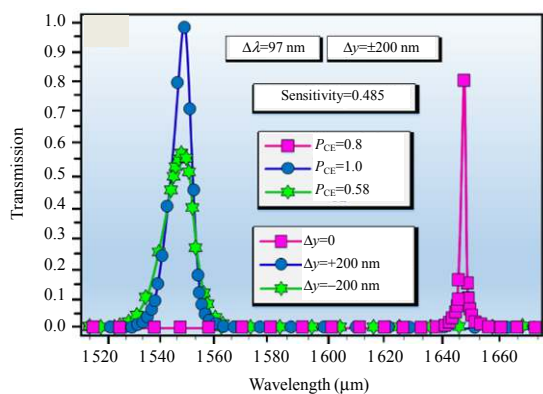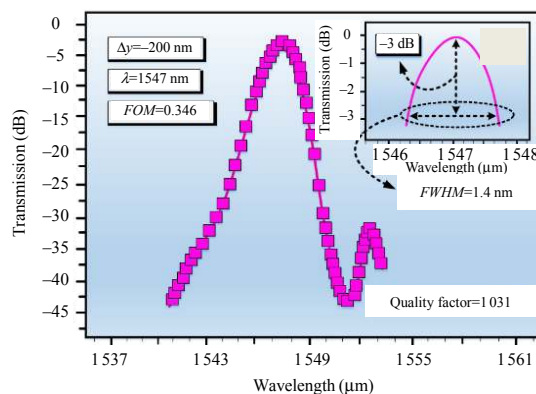

(a)
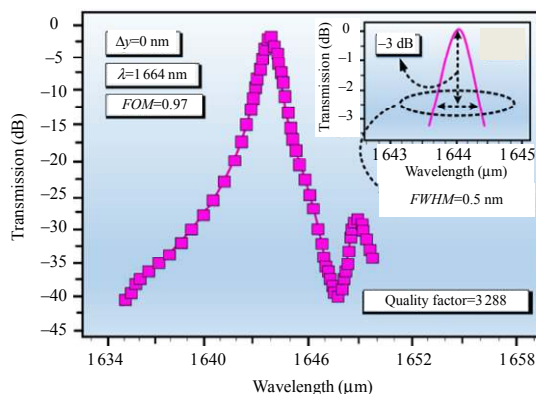
(b)

(c)

(d)

Fig. 6 Results of (a) transmission spectra of Case-A, Case-D, and Case-E, and transmission in dB of (b) Case-A, (c) Case-D, and (d) Case-E.

Mojtaba HOSSEINZADEH SANI *et al.*: A Novel All-Optical Sensor Design Based on a Tunable Resonant Nanocavity in Photonic Crystal Microstructure Applicable in MEMS Accelerometers
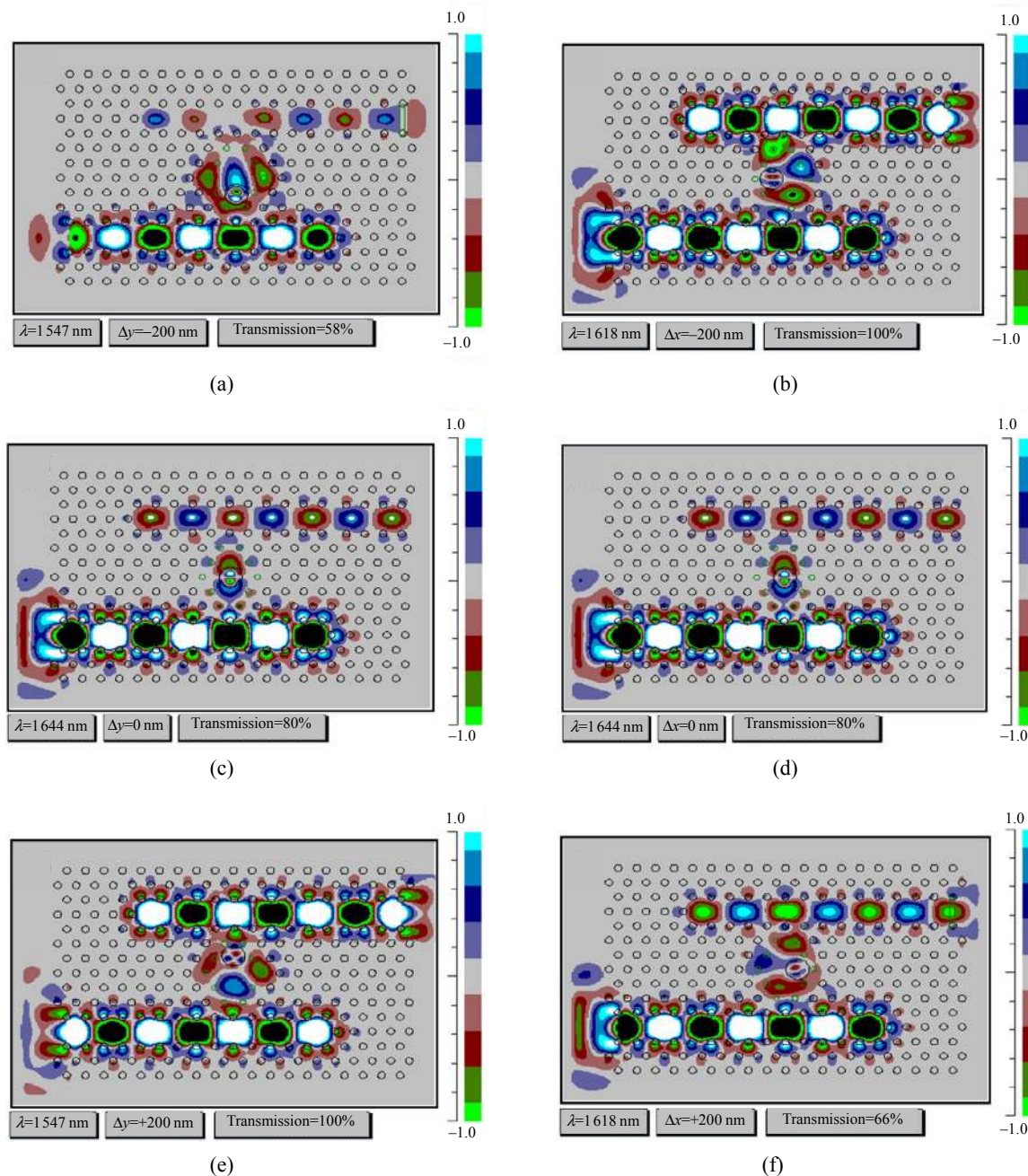
465

(a)

(b)

(c)

(d)

(e)

(f)

Fig. 7 Lightwave propagation inside the AOS for nanocavity displacements in x- or y-direction.

To accurately calculate the parameters of the proposed structure, we obtain the resonance wavelength and *FWHM* from −200 nm to 200 nm with steps of 50 nm along the *x*- or *y*-direction. As can be observed in Fig. 8, when the nanocavity is stationary in the center of the structure, the maximum resonance wavelength and the minimum *FWHM* are obtained. It means that the non-displacement of the nanocavity in the *xy*-plane (i.e., Δ*x*=0 and Δ*y*=0) leads to a maximum resonant wavelength of 1.644 μm and the narrowest spectrum with *FWHM* of 0.5 nm at the output. Figure 8(a) reveals that the resonant wavelength variations of the sensor with the nanocavity displacement in the *x*-direction are in the range of 1.618 μm to 1.644 μm, which are less than those presented in Fig. 8(b) for the displacement in the *y*-direction.
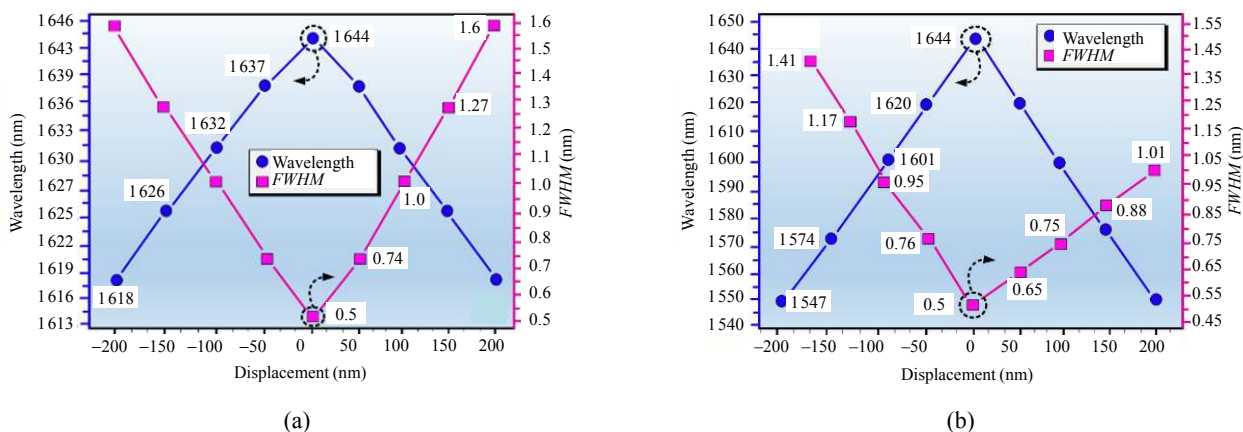
(a)

(b)

Fig. 8 Resonant wavelength and *FWHM* parameters of the nanocavity displacements in the (a) *x*-direction and (b) *y*-direction.

Furthermore, Fig. 8 illustrates that *FWHMs* are in the range of 0.5 nm to 1.6 nm for the nanocavity displacement in the *x*-direction, while they are in the range of 0.5 nm to 1.35 nm depending on the nanocavity displacement in the *y*-direction. The sensitivity is a key parameter to determine the performance of an optical sensor. In this section, the sensitivity is calculated for different displacements in the (a) *x*- and (b) *y*-directions. The sensitivities of 50 nm, 100 nm, and 150 nm nanocavity displacements along the *x*-axis and *y*-axis are plotted in Fig. 9. According to Fig. 9(a), when the displacement of the nanocavity along the *x*-axis is about 50 nm, the maximum sensitivity of 0.16 nm is achieved. The lowest sensitivity occurs when the central nanocavity displacement is about 150 nm along the *x*-axis. Figure 9(b) demonstrates the maximum sensitivity is 0.48 for the central nanocavity displacement of 100 nm along the *y*-axis.
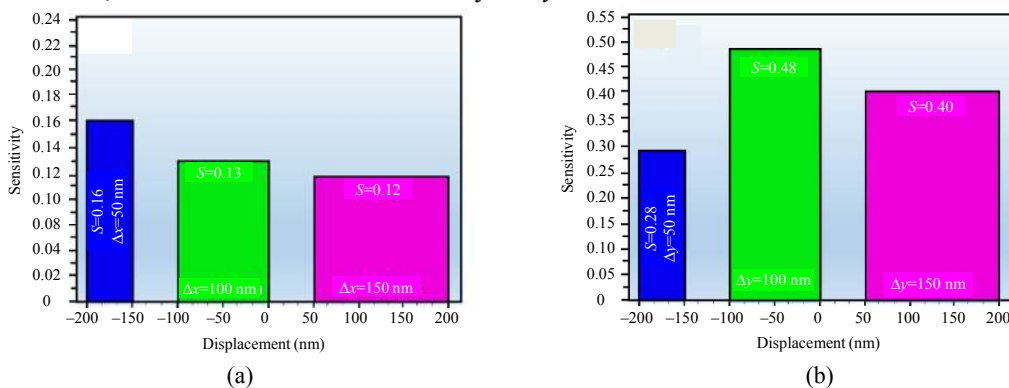

(a)

(b)

Fig. 9 Sensitivities of 50 nm, 100 nm, and 150 nm nanocavity displacements along the (a) *x*-axis and (b) *y*-axis.
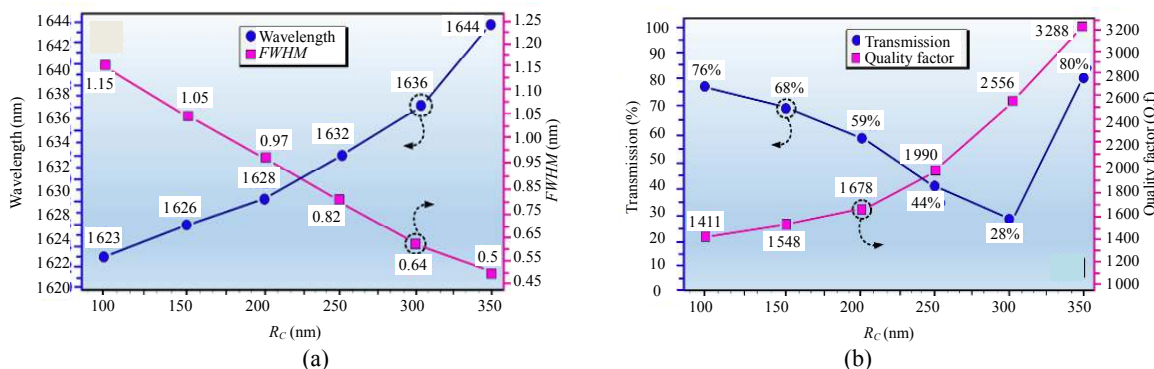

(a)

(b)

Fig. 10 Results of (a) resonant wavelength and *FWHM* versus nanocavity radius and (b) quality factor and the transmission versus nanocavity radius.

In order to obtain the most appropriate central nanocavity radius, we calculate the important parameters of the structure for different central nanocavity radii in Case-A (non-displacement of the nanocavity in the *xy*-plane, i.e., Δx=0 and Δy=0). Figure 10(a) shows the resonant wavelength and *FWHM* for different radii of the central resonant nanocavity. It illustrates that as the radius of the central nanocavity increases, the resonant wavelength increases and *FWHM* decreases. Therefore, we set the radius of the central nanocavity to 350 nm. In this way, *FWHM* reaches to the lowest value of 0.5 nm, which means the proposed AOS is a frequency selective sensor with the high sensitivity and accuracy. Figure 10(b) shows the quality factor and transmission as a function of the central rod radii. It reveals that the maximum quality factor of 3 288 is achieved at a radius of 350 nm. On the other hand, the maximum transmission of 80% is also obtained in this radius. Therefore, R_C = 350 nm is an appropriate choice for the proposed AOS.

According to the equations of the sensors and filters mentioned in Section 4, there is a compromise between the sensitivity and the measurement range, and the proposed sensor in this study is designed to provide a broader measurement range with a suitable optical sensitivity compared with other recently published papers. This comparative study is summarized in Table 1.

Table 1 Comparative table of the proposed sensor and three important recent contributions.

	This work	Ref. [76]	Ref. [64]	Ref. [58]	Ref. [84]	Ref. [85]	Ref. [82]
Sensitivity of the sensing system ($\Delta\lambda/\Delta y$)	0.485	0.0472	1.23–1.41	0.368	0.032	0.069	3
Operating band width (nm)	High	High	High	Medium	Low	Low	Very high

5. Conclusions

In summary, we design a novel MEMS accelerometer sensor utilizing an ultrafast AOS in a two-dimensional hexagonal PhC structure. The fundamental PhC consists of a 19×13 matrix of silicon rods with a 100 nm rod radius and a 500 nm lattice constant. The proposed AOS includes a ring resonator with a movable rod (connected to the proof mass by a holder) at the center of the ring and two fixed waveguides in the PhC platform with an area of 104.35 µm². We calculate the characteristics of the AOS for nanocavity displacements in the *x*-direction and *y*-direction from –200 nm to 200 nm with steps of 50 nm. Numerical results demonstrate that the AOS has a resonant peak of 0.8 at 1.644 µm, a quality factor of 3 288, *FWHM* of 0.5 nm, and *FOM* of 0.97 for the non-displacement of the nanocavity. We also compute those parameters for the maximum displacements of ±200 nm in the *x*-direction and *y*-direction. Simulations reveal to achieve the maximum quality factor and the minimum *FWHM*, and the best radius of the central rod in the resonator is 350 nm. Simulations also demonstrate that the proposed AOS has the sensitivities of 0.13 and 0.485 for the displacements of 200 nm in the *x*-direction and *y*-direction, respectively. These functional characteristics make the proposed AOS appeal for several applications in the navigation systems and safety tools.

Acknowledgment

References

[1] C. M. Soukoulis, *Photonic crystals and light localization in the 21st century*. Germany: Springer

Science & Business Media, 2001: 563.

[2]   K. Sakoda, *Optical properties of photonic crystals.* Germany: Springer Science & Business Media, 2001: 80.

[3]   M. R. Rakhshani and M. A. Mansouri-Birjandi, "Realization of tunable optical filter by photonic crystal ring resonators," *Optik*, 2013, 124(22): 5377–5380.

[4]   S. Naghizade and S. M. Sattari-Esfahlan, "Excellent quality factor ultra-compact optical communication filter on ring-shaped cavity," *Journal of Optical Communications*, 2019, 40(1): 21–25.

[5]   S. Naghizade and S. M. Sattari-Esfahlan, "Loss-less elliptical channel drop filter for WDM applications," *Journal of Optical Communications*, 2019, 40(4): 379–384.

[6]   M. A. Mansouri-Birjandi, A. Tavousi, and M. Ghadrdan, "Full-optical tunable add/drop filter based on nonlinear photonic crystal ring resonators," *Photonics and Nanostructures – Fundamentals and Applications*, 2016, 21: 44–51.

[7]   M. Hosseinzadeh Sani, A. Ghanbari, and H. Saghaei, "An ultra-narrowband all-optical filter based on the resonant cavities in rod-based photonic crystal microstructure," *Optical and Quantum Electronics*, 2020, 52(6): 295.

[8]   S. Naghizade and H. Saghaei, "Tunable graphene-on-insulator band-stop filter at the mid-infrared region," *Optical and Quantum Electronics*, 2020, 52(4): 224.

[9]   M. Ebnali-Heidari, H. Saghaei, F. Koohi-Kamali, M. Naser Moghadasi, and M. K. Moravvej-Farshi, "Proposal for supercontinuum generation by optofluidic infiltrated photonic crystal fibers," *IEEE Journal on Selected Topics in Quantum Electronics*, 2014, 20(5): 582–589.

[10] H. Saghaei, "Dispersion-engineered microstructured optical fiber for mid-infrared supercontinuum generation," *Applied Optics*, 2018, 57(20): 5591–5598.

[11] H. Saghaei, M. Ebnali-Heidari, and M. K. Moravvej-Farshi, "Midinfrared supercontinuum generation via As$_2$Se$_3$ chalcogenide photonic crystal fibers," *Applied Optics*, 2015, 54(8): 2072–2079.

[12] H. Saghaei and A. Ghanbari, "White light generation using photonic crystal fiber with sub-micron circular lattice," *Journal of Electrical Engineering*, 2017, 68(4): 282–289.

[13] A. Kowsari and H. Saghaei, "Resonantly enhanced all-optical switching in microfibre Mach-Zehnder interferometers," *Electronics Letters*, 2018, 54(4): 229–231.

[14] M. Aliee, M. H. Mozaffari, and H. Saghaei, "Dispersion-flattened photonic quasicrystal optofluidic fiber for telecom C band operation," *Photonics and Nanostructures – Fundamentals and Applications*, 2020, 40: 100797.

[15] S. Naghizade and H. Saghaei, "A novel design of all-optical 4 to 2 encoder with multiple defects in silica-based photonic crystal fiber," *Optik*, 2020, 222: 165419.

[16] A. Ghanbari, A. Kashaninia, A. Sadr, and H. Saghaei, "Supercontinuum generation for optical coherence tomography using magnesium fluoride photonic crystal fiber," *Optik*, 2017, 140: 545–554.

[17] R. Raei, M. Ebnali-Heidari, and H. Saghaei, "Supercontinuum generation in organic liquid-liquid core-cladding photonic crystal fiber in visible and near-infrared regions," *Journal of the Optical Society of America B*, 2018, 35(2): 323–330.

[18] M. Kalantari, A. Karimkhani, and H. Saghaei, "Ultra-wide mid-IR supercontinuum generation in As$_2$S$_3$ photonic crystal fiber by rods filling technique," *Optik*, 2018, 158(24): 142–151.

[19] F. Mehdizadeh, M. Soroosh, and H. Alipour-Banaei, "An optical demultiplexer based on photonic crystal ring resonators," *Optik*, 2016, 127(20): 8706–8709.

[20] S. Naghizade and S. M. Sattari-Esfahlan, "High-performance ultra-compact communication triplexer on silicon-on-insulator photonic crystal structure," *Photonic Network Communications*, 2017, 34(3): 445–450.

[21] F. Mehdizadeh and M. Soroosh, "A new proposal for eight-channel optical demultiplexer based on photonic crystal resonant cavities," *Photonic Network Communications*, 2016, 31(1): 65–70.

[22] S. Naghizade and S. M. Sattari-Esfahlan, "An optical five channel demultiplexer-based simple photonic crystal ring resonator for WDM applications," *Journal of Optical Communications*, 2018, 41(1): 37–43.

[23] M. R. Rakhshani and M. A. Mansouri-Birjandi, "Design and simulation of four-channel wavelength demultiplexer based on photonic crystal circular ring resonators for optical communications," *Journal of Optical Communications*, 2014, 35(1): 9–15.

[24] S. Asgari and N. Granpayeh, "Tunable plasmonic dual wavelength multi/demultiplexer based on graphene sheets and cylindrical resonator," *Optics Communications*, 2017, 393: 5–10.

[25] G. Manzacca, D. Paciotti, A. Marchese, M. S. Moreolo, and G. Cincotti, "2D photonic crystal cavity-based WDM multiplexer," *Photonics and Nanostructures-Fundamentals and Applications*, 2007, 5(4): 164–170.

[26] H. Saghaei, "Supercontinuum source for dense wavelength division multiplexing in square photonic crystal fiber via fluidic infiltration approach," *Radioengineering*, 2017, 26(1): 16–22.

[27] T. A. Moniem, "All-optical digital 4 × 2 encoder based on 2D photonic crystal ring resonators," *Journal of Modern Optics*, 2016, 63(8): 735–741.

[28] F. Mehdizadeh, M. Soroosh, and H. Alipour-Banaei, "Proposal for 4-to-2 optical encoder based on

Mojtaba HOSSEINZADEH SANI *et al.*: A Novel All-Optical Sensor Design Based on a Tunable Resonant Nanocavity in
Photonic Crystal Microstructure Applicable in MEMS Accelerometers

469

photonic crystals," *IET Optoelectronics*, 2017, 11(1): 29–35.

[29] S. Salimzadeh and H. Alipour-Banaei, "A novel proposal for all optical 3 to 8 decoder based on nonlinear ring resonators," *Journal of Modern Optics*, 2018, 65(17): 2017–2024.

[30] H. Alipour-Banaei, F. Mehdizadeh, S. Serajmohammadi, and M. Hassangholizadeh-Kashtiban, "A 2*4 all optical decoder switch based on photonic crystal ring resonators," *Journal of Modern Optics*, 2015, 62(6): 430–434.

[31] F. Mehdizadeh, M. Soroosh, and H. Alipour-Banaei, "A novel proposal for optical decoder switch based on photonic crystal ring resonators," *Optical and Quantum Electronics*, 2016, 48(1): 1–9.

[32] D. M. Beggs, T. P. White, L. Cairns, L. O'Faolain, and T. F. Krauss, "Demonstration of an integrated optical switch in a silicon photonic crystal directional coupler," *Physica E: Low-Dimensional Systems and Nanostructures*, 2009, 41(6): 1111–1114.

[33] H. Saghaei, A. Zahedi, R. Karimzadeh, and F. Parandin, "Line defects on As$_2$Se$_3$-chalcogenide photonic crystals for the design of all-optical power splitters and digital logic gates," *Superlattices and Microstructures*, 2017, 110: 133–138.

[34] H. Saghaei and V. Van, "Broadband mid-infrared supercontinuum generation in dispersion-engineered silicon-on-insulator waveguide," *Journal of the Optical Society of America B*, 2019, 36(2): A193–A202.

[35] H. Saghaei, P. Elyasi, and R. Karimzadeh, "Design, fabrication, and characterization of Mach-Zehnder interferometers," *Photonics and Nanostructures – Fundamentals and Applications*, 2019, 37: 100733.

[36] M. Diouf, A. Ben Salem, R. Cherif, H. Saghaei, and A. Wague, "Super-flat coherent supercontinuum source in As$_{38.8}$Se$_{61.2}$ chalcogenide photonic crystal fiber with all-normal dispersion engineering at a very low input energy," *Applied Optics*, 2017, 56(2): 163–169.

[37] A. Salmanpour, S. Mohammadnejad, and P. T. Omran, "All-optical photonic crystal NOT and OR logic gates using nonlinear Kerr effect and ring resonators," *Optical and Quantum Electronics*, 2015, 47(12): 3689–3703.

[38] M. M. Karkhanehchi, F. Parandin, and A. Zahedi, "Design of an all optical half-adder based on 2D photonic crystals," *Photonic Network Communications*, 2017, 33(2): 159–165.

[39] A. M. Vali-Nasab, A. Mir, and R. Talebzadeh, "Design and simulation of an all optical full-adder based on photonic crystals," *Optical and Quantum Electronics*, 2019, 51(5): 161.

[40] M. H. Sani, A. A. Tabrizi, H. Saghaei, and R. Karimzadeh, "An ultrafast all-optical half adder using nonlinear ring resonators in photonic crystal

microstructure," *Optical and Quantum Electronics*, 2020, 52(2): 107.

[41] S. Naghizade and H. Saghaei, "A novel design of all-optical half adder using a linear defect in a square lattice rod-based photonic crystal microstructure," *arXiv preprint arXiv:2002.04535*, 2020.

[42] F. Parandin, M. M. Karkhanehchi, M. Naseri, and A. Zahedi, "Design of a high bitrate optical decoder based on photonic crystals," *Journal of Computational Electronics*, 2018, 17(2): 830–836.

[43] A. Tavousi, M. A. Mansouri-Birjandi, and M. Saffari, "Successive approximation-like 4-bit full-optical analog-to-digital converter based on Kerr-like nonlinear photonic crystal ring resonators," *Physica E: Low-Dimensional Systems and Nanostructures*, 2016, 83: 101–106.

[44] K. Fasihi, "All-optical analog-to-digital converters based on cascaded 3-dB power splitters in 2D photonic crystals," *Optik*, 2014, 125(21): 6520–6523.

[45] F. Mehdizadeh, M. Soroosh, H. Alipour-Banaei, and E. Farshidi, "All optical 2-bit analog to digital converter using photonic crystal based cavities," *Optical and Quantum Electronics*, 2017, 49(1): 38.

[46] B. Youssefi, M. K. Moravvej-Farshi, and N. Granpayeh, "Two bit all-optical analog-to-digital converter based on nonlinear Kerr effect in 2D photonic crystals," *Optics Communications*, 2012, 285(13–14): 3228–3233.

[47] M. H. Sani, S. Khosroabadi, and M. Nasserian, "High performance of an all-optical two-bit analog-to-digital converter based on Kerr effect nonlinear nanocavities," *Applied Optics*, 2020, 59(4): 1049–1057.

[48] M. H. Sani, S. Khosroabadi, and A. Shokouhmand, "A novel design for 2-bit optical analog to digital (A/D) converter based on nonlinear ring resonators in the photonic crystal structure," *Optics Communications*, 2020, 458: 124760.

[49] A. Tavousi and M. A. Mansouri-Birjandi, "Optical-analog-to-digital conversion based on successive-like approximations in octagonal-shape photonic crystal ring resonators," *Superlattices and Microstructures*, 2018, 114: 23–31.

[50] R. V. Nair and R. Vijaya, "Photonic crystal sensors: An overview," *Progress in Quantum Electronics*, 2010, 34(3): 89–134.

[51] J. Jágerská, H. Zhang, Z. Diao, N. Le Thomas, and R. Houdré, "Refractive index sensing with an air-slot photonic crystal nanocavity," *Optics Letters*, 2010, 35(15): 2523–2525.

[52] F. Tavakoli, F. B. Zarrabi, and H. Saghaei, "Modeling and analysis of high-sensitivity refractive index sensors based on plasmonic absorbers with Fano response in the near-infrared spectral region," *Applied Optics*, 2019, 58(20): 5404–5414.

[53] Y. Liu and H. W. M. Salemink, "Photonic

crystal-based all-optical on-chip sensor," *Optics Express*, 2012, 20(18): 19912–19920.

[54] M. H. Sani and S. Khosroabadi, "A novel design and analysis of high-sensitivity biosensor based on nano-cavity for detection of blood component, diabetes, cancer and glucose concentration," *IEEE Sensors Journal*, 2020, 20(13): 7161–7168.

[55] A. A. Tabrizi and A. Pahlavan, "Efficiency improvement of a silicon-based thin-film solar cell using plasmonic silver nanoparticles and an antireflective layer," *Optics Communications*, 2020, 454: 124437.

[56] H. Saghaei, V. Heidari, M. Ebnali-Heidari, and M. R. Yazdani, "A systematic study of linear and nonlinear properties of photonic crystal fibers," *Optik*, 2016, 127(24): 11938–11947.

[57] H. Saghaei, M. K. Moravvej-Farshi, M. Ebnali-Heidari, and M. N. Moghadasi, "Ultra-wide mid-infrared supercontinuum generation in $As_{40}Se_{60}$ chalcogenide fibers: solid core PCF versus SIF," *IEEE Journal of Selected Topics in Quantum Electronics*, 2016, 22(2): 279–286.

[58] A. Sheikhaleh, K. Abedi, and K. Jafari, "A proposal for an optical MEMS accelerometer relied on wavelength modulation with one dimensional photonic crystal," *Journal of Lightwave Technology*, 2016, 34(22): 5244–5249.

[59] A. G. Krause, M. Winger, T. D. Blasius, Q. Lin, and O. Painter, "A high-resolution microchip optomechanical accelerometer," *Nature Photonics*, 2012, 6(11): 768–772.

[60] T. Ke, T. Zhu, Y. Rao, and M. Deng, "Accelerometer based on all-fiber Fabry-Pérot interferometer formed by hollow-core photonic crystal fiber," *Microwave and Optical Technology Letters*, 2010, 52(11): 2531–2535.

[61] D. K. Shaeffer, "MEMS inertial sensors: a tutorial overview," *IEEE Communications Magazine*, 2013, 51(4): 100–109.

[62] Y. Li, M. Efatmaneshnik, and A. G. Dempster, "Attitude determination by integration of MEMS inertial sensors and GPS for autonomous agriculture applications," *GPS Solutions*, 2012, 16(1): 41–52.

[63] J. Cheng, J. Dong, R. Landry Jr, and D. Chen, "A novel optimal configuration form redundant MEMS inertial sensors based on the orthogonal rotation method," *Sensors*, 2014, 14(8): 13661–13678.

[64] K. Huang, L. Cao, P. Zhai, P. Liu, L. Cheng, and J. Liu, "High sensitivity sensing system theoretical research base on waveguide-nano DBRs one dimensional photonic crystal microstructure," *Optics Communications*, 2020, 470: 125392.

[65] K. Huang, M. Yu, L. Cheng, J. Liu, and L. Cao, "A proposal for an optical MEMS accelerometer with high sensitivity based on wavelength modulation system," *Journal of Lightwave Technology*, 2019, 37(21): 5474–5478.

[66] H. Sun, D. Fang, K. Jia, F. Maarouf, H. Qu, and H. Xie, "A low-power low-noise dual-chopper amplifier for capacitive CMOS-MEMS accelerometers," *IEEE Sensors Journal*, 2010, 11(4): 925–933.

[67] R. Xu, S. Zhou, and W. J. Li, "MEMS accelerometer based nonspecific-user hand gesture recognition," *IEEE Sensors Journal*, 2012, 12(5): 1166–1173.

[68] A. Albarbar, A. Badri, J. K. Sinha, and A. Starr, "Performance evaluation of MEMS accelerometers," *Measurement: Journal of the International Measurement Confederation*, 2009, 42(5): 790–795.

[69] W. Noell, P. A. Clerc, L. Dellmann, B. Guldimann, H. P. Herzig, O. Manzardo, *et al.*, "Applications of SOI-based optical MEMS," *IEEE Journal on Selected Topics in Quantum Electronics*, 2002, 8(1): 148–154.

[70] E. Ollier, "Optical MEMS devices based on moving waveguides," *IEEE Journal on Selected Topics in Quantum Electronics*, 2002, 8(1): 155–162.

[71] M. C. Wu, O. Solgaard, and J. E. Ford, "Optical MEMS for lightwave communication," *Journal of Lightwave Technology*, 2006, 24(12): 4433–4454.

[72] S. Kavitha, R. Joseph Daniel, and K. Sumangala, "Design and analysis of MEMS comb drive capacitive accelerometer for SHM and seismic applications," *Measurement: Journal of the International Measurement Confederation*, 2016, 93: 327–339.

[73] C. Acar and A. M. Shkel, "Experimental evaluation and comparative analysis of commercial variable-capacitance MEMS accelerometers," *Journal of Micromechanics and Microengineering*, 2003, 13(5): 634–645.

[74] A. Walther, M. Savoye, G. Jourdan, P. Renaux, F. Souchon, P. Robert, *et al.*, "3-axis gyroscope with Si nanogage piezo-resistive detection," in *2012 IEEE 25th International Conference on Micro Electro Mechanical Systems (MEMS)*, Paris, Jan. 29–Feb. 2, 2012, pp. 480–483.

[75] J. C. Yu and C. B. Lan, "System modeling of microaccelerometer using piezoelectric thin films," *Sensors and Actuators, A: Physical*, 2001, 88(2): 178–186.

[76] A. Sheikhaleh, K. Abedi, and K. Jafari, "An optical MEMS accelerometer based on a two-dimensional photonic crystal add-drop filter," *Journal of Lightwave Technology*, 2017, 35(14): 3029–3034.

[77] K. Zandi, B. Wong, J. Zou, R. V Kruzelecky, W. Jamroz, and Y. A. Peter, "In-plane silicon-on-insulator optical MEMS accelerometer using waveguide fabry-perot microcavity with silicon/air bragg mirrors," in *2010 IEEE 23rd International Conference on Micro Electro Mechanical Systems (MEMS)*, Hong Kong, Jan. 24–28, 2010, pp. 839–842.

[78] H. Luo, G. Zhang, L. R. Carley, and G. K. Fedder, "A post-CMOS micromachined lateral accelerometer,"

Mojtaba HOSSEINZADEH SANI *et al.*: A Novel All-Optical Sensor Design Based on a Tunable Resonant Nanocavity in
Photonic Crystal Microstructure Applicable in MEMS Accelerometers

471

Journal of Microelectromechanical Systems, 2002,
11(3): 188–195.

[79] J. Wu, G. K. Fedder, and L. R. Carley, "A low-noise
low-offset capacitive sensing amplifier for a
50-/spl mu/g//spl radic/Hz monolithic CMOS
MEMS accelerometer," *IEEE Journal of Solid-State
Circuits*, 2004, 39(5): 722–730.

[80] E. Soltanian, K. Jafari, and K. Abedi, "A novel
differential optical MEMS accelerometer based on
intensity modulation, using an optical power
splitter," *IEEE Sensors Journal*, 2019, 19(24):
12024–12030.

[81] M. Ahmadian and K. Jafari, "A graphene-based
wide-band MEMS accelerometer sensor dependent
on wavelength modulation," *IEEE Sensors Journal*,
2019, 19(15): 6226–6232.

[82] Y. Nie, K. Huang, J. Yang, L. Cao, L. Cheng, Q.
Wang, *et al.*, "A proposal to enhance high-frequency

optical MEMS accelerometer sensitivity based on a
one-dimensional photonic crystal wavelength
modulation system," *IEEE Sensors Journal*, 2020: 1.

[83] S. Olyaee, H. Mohsenirad, and A. Mohebzadeh-
Bahabady, *Photonic crystal chemical/biochemical
sensors*, in *Progresses in Chemical Sensor*, Croatia:
IntechOpen, 2016: Ch. 3.

[84] C. Trigona, B. Ando, and S. Baglio, "Design,
fabrication, and characterization of BESOI-
accelerometer exploiting photonic bandgap
materials," *IEEE Transactions on Instrumentation
and Measurement*, 2014, 63(3): 702–710.

[85] K. Zandi, J. A. Bélanger, and Y. A. Peter, "Design
and demonstration of an in-plane silicon-on-insulator
optical MEMS Fabry-Pérot-based accelerometer
integrated with channel waveguides," *Journal of
Microelectromechanical Systems*, 2012, 21(6):
1464–1470.